BIOSENSORS

Active-reset protein sensors enable continuous in vivo monitoring of inflammation

H. Zargartalebi[1,2,3], S. Mirzaie[3], A. GhavamiNejad[1], S. U. Ahmed[1,4], F. Esmaeili[2,5], A. Geraili[3], C. D. Flynn[2], D. Chang[1], J. Das[2], A. Abdrabou[4,6], E. H. Sargent[2,5,7], S. O. Kelley[1,2,3,4,6]*

Continuous measurement of proteins in vivo is important for real-time disease management and prevention. Implantable sensors for monitoring small molecules such as glucose have been available for more than a decade. However, analysis of proteins remains an unmet need because the lower physiological levels require that sensors have high affinities, which are linked to long complexation half-lives ($t_{1/2}$ ~20 hours) and slow equilibration when concentrations decrease. We report active-reset sensors by use of high-frequency oscillations to accelerate dissociation, which enables regeneration of the unbound form of the sensor within 1 minute. When implemented within implanted devices, these sensors allow for real-time, in vivo monitoring of proteins within interstitial fluid. Active-reset protein sensors track biomarker levels on a physiological timescale for inflammation monitoring in living animals.

The development of wearable and implantable sensors for health-related biomarkers has the potential to revolutionize disease monitoring and prevention (1, 2). The ability to continuously measure protein biomarker concentrations in bodily fluids would enable the tracking of patients at risk of acute, rapid deterioration as well as those managing chronic diseases (3–5). Moreover, the ever-emerging role of inflammation in all aspects of human health indicates that real-time monitoring could be pivotal in preventing many major health issues, including heart disease (6), diabetes (7), and even depression (8).

Previously reported body-interfaced (wearable or implantable) sensors are mainly restricted to monitoring of small molecules, such as electrolytes (9, 10), drugs (11–13), neurotransmitters (14–16), hormones (17–19), and metabolites (20–22). Continuous, in vivo protein monitoring has remained a substantial challenge given that many sensing strategies require reagents or reporter groups that are incompatible with the development of self-contained sensing devices for use on or inside the human body. Although progress is being made in the area of reagentless protein-sensing systems (23, 24), existing systems remain incompatible with dynamic measurements of proteins in vivo. The detection of the low levels of proteins present in physiological media requires the use of affinity receptors, such as antibodies and aptamers. These have long dissociation times that prohibit real-time tracking of decreasing protein levels (1, 25–27). For example, affinity receptors that exhibit dissociation constant (K_d) values of 1 nM may have dissociation rates of 10^{-5} s^{-1} and complexation half-lives of ~20 hours. Slow dissociation kinetics impede the ability of sensors to dynamically respond to and report on changes in protein levels. Although previous studies have explored tracking protein biomarker levels in vivo, including in excreted fluids such as sweat (26, 28–30), real-time monitoring of changes in live animals has remained an unmet need.

Biomolecular analysis approach

We reasoned that the wait time for passive complex dissociation to occur underlies the slowness of sensor response, but that an active approach, in which an external stimulus was applied to force dissociation, could break through this bottleneck. A reagentless molecular pendulum (31–33) that uses a tethered DNA sensor construct for temporally differentiated Faradaic readout (Fig. 1A) was used as the starting point for the development of an implantable sensor for continuous protein monitoring (Fig. 1B). This construct consists of a rigid, electrode-bound double-stranded DNA scaffold with a terminal ferrocene molecule (e⁻ donor) and protein aptamer sequence. Aptamers were selected as receptors in this system owing to their programmable interactions, small physical size, high stability, and long shelf life, making them ideal candidates for highly sensitive and selective in vivo protein monitoring (34–37). The application of +500 mV (versus silver) draws DNA to the electrode, where ferrocene is oxidized. Protein detection occurs by observing delayed oxidation due to hydrodynamic drag that affects electron-transfer rates. The pendulum sensing approach has previously been used for reagentless protein monitoring in situ (31–33) but, given the slow timescale of passive reset, could not resolve changing protein centrations in real time.

This sensing approach is reagentless because it does not require the addition of reporter groups or other additives and is therefore suited for the development of implantable protein sensing devices (Fig. 1C). The aptamer portion of the sensor is a modular element that can be substituted to allow the development of constructs for different protein analytes. High levels of sensitivity and specificity for a range of analytes can be achieved in simulated interstitial fluid (ISF) by using this approach (figs. S1 to S4) that match the requirements of physiological monitoring. However, the high-affinity receptors that are used to achieve the needed levels of sensitivity are associated with long dissociation times, which requires the development of an active-reset mechanism to ensure that sensors can report on both increases and decreases in concentration.

Development of sensor reset approach for continuous protein measurements

When a protein interacts with the aptamer-based receptor, the rate of electron transfer between the sensor-appended redox label and the electrode surface is slowed because of the altered hydrodynamic drag for molecular pendulum methodology. This electron-transfer delay manifests as a decrease in current decay in chronoamperometry (Fig. 2A), allowing for the correlation of the change in current at a given time point (ΔI) with protein concentration. The measurement of sensor response when three aptamers with varying dissociation constants (aptamer sequences and sources are provided in table S1) for a model analyte [myeloperoxidase (MPO)] of 27 nM (low affinity), 2 nM (moderate affinity), and 160 pM (high affinity) are used (27) illustrates the need for an active-reset mechanism (Fig. 2B). When a protein-containing solution was substituted with buffer (passive reset), the signal changes observed among aptamers were 70% (low affinity), 30% (medium affinity), and 5% (high affinity) after 30 min of incubation. Despite the lack of protein target in solution, the sensor with picomolar affinity to the protein was unable to report on this pronounced concentration change.

Although programming receptors for higher dissociation rates is one method of reducing dissociation times, this approach may adversely affect receptor sensitivity and selectivity. We instead present a more active form of analyte dissociation and sensor reset by using an oscillation-based approach. We hypothesized that by inducing rapid oscillation of the sensor through changes in potential and applied electric field, the drag and inertial forces induced might cause the target protein to rapidly dissociate when concentrations dropped below K_d. As shown in Fig. 2C, applying +0.3 V at 95 Hz resets the sensor in <1 min, as confirmed with

[1]Department of Biomedical Engineering, McCormick School of Engineering, Northwestern University, Evanston, IL, USA. [2]Department of Chemistry, Weinberg College of Arts and Sciences, Northwestern University, Evanston, IL, USA. [3]Department of Pharmaceutical Sciences, Leslie Dan Faculty of Pharmacy, University of Toronto, Toronto, ON, Canada. [4]Robert H. Laurie Comprehensive Cancer Center, Northwestern University, Chicago, IL, USA. [5]Department of Electrical and Computer Engineering, University of Toronto, Toronto, ON, Canada. [6]Chan Zuckerberg Biohub Chicago, Chicago, IL, USA. [7]Department of Electrical and Computer Engineering, Northwestern University, Evanston, IL, USA.
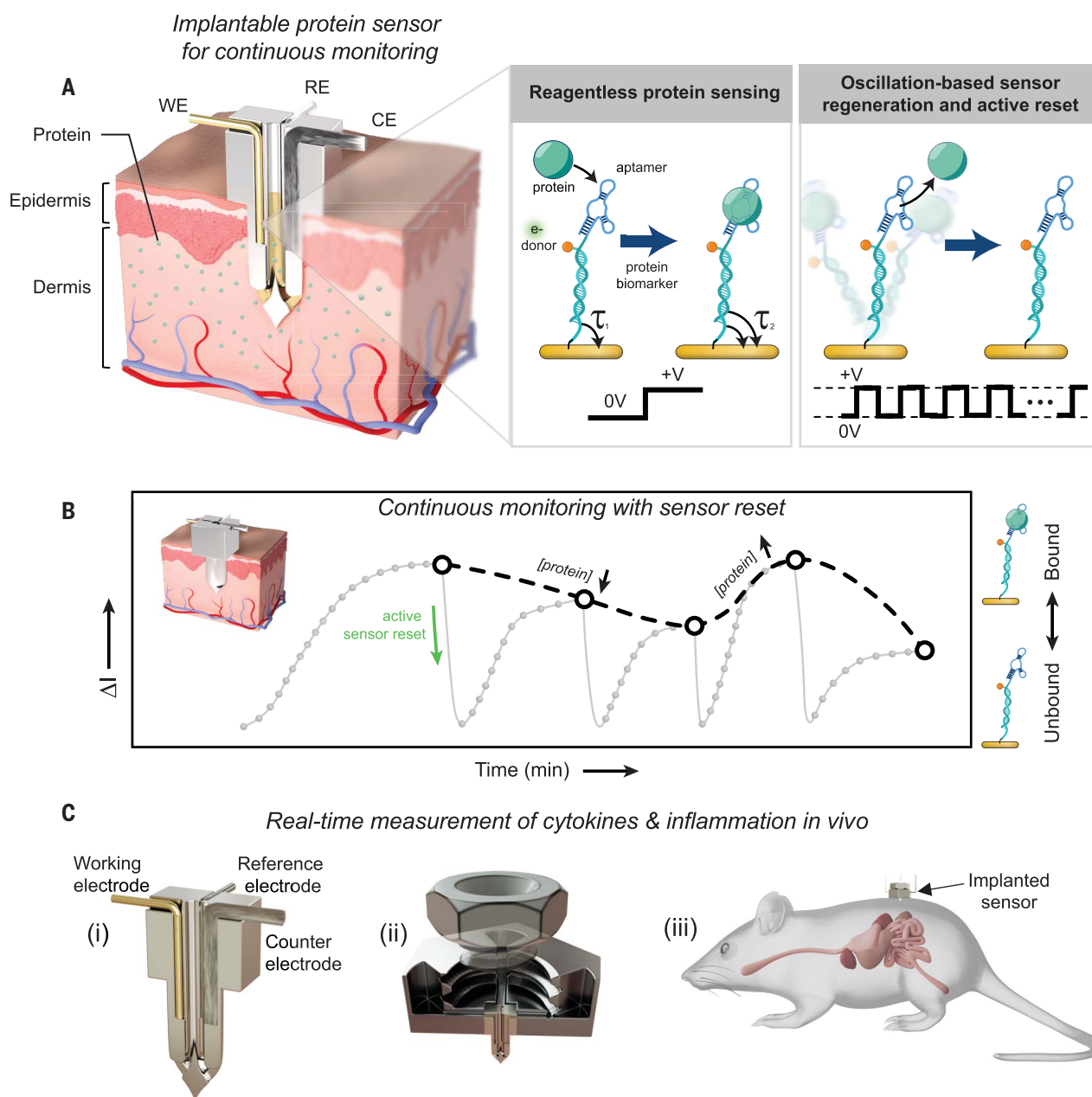*Corresponding author. Email: shana.kelley@northwestern.edu

Fig. 1. Active-reset sensors for continuous protein monitoring in vivo.
(**A**) (Left) Schematic of microdevice inserted into skin. The device delivers ISF to the working electrode (WE), reference electrode (RE), and counter electrode (CE) upon insertion into the skin. (Middle) Aptamer-based molecular pendulum sensors enable reagentless analysis of protein biomarkers ($\tau_2 > \tau_1$). (Right) Potential-mediated oscillation enables active reset of sensors. Application of an alternating potential results in oscillation of the molecular pendulum constructs and subsequent release of target proteins. (**B**) The oscillatory-based sensor reset method enables continuous monitoring of increasing and decreasing protein levels. (**C**) Microdevice design and application. (i) Electrode-integrated microdevice and internal features. (ii) Design of the capillary-based microdevice along with subcomponents needed for in vivo monitoring. (iii) Schematic of the implanted sensor mounted on a rat for real-time, in vivo cytokine monitoring.

electrochemical analysis. Quartz crystal microbalance (QCM) measurements validated this reset, with frequency difference (Δf) values after the reset matching phosphate-buffered saline (PBS)–only values, which indicates complete analyte displacement (Fig. 2D and fig. S5). Negative alternating potentials have no significant effect on the bound signal (fig. S6). The reset methodology is versatile for aptamers with various affinities by adjusting voltage and frequency (fig. S7), with multiple reset cycles feasible without significant degradation (figs. S8 to S12). The extent of reset or dissociation can be controlled by varying voltage and frequency (Fig. 2E). There is also a strong correlation between aptamer affinity and the reset parameters, highlighting the method's adaptability for different aptamer-target complexes (Fig. 2F).

Using this sensor reset approach, we challenged the platform to monitor MPO for more than 700 min, with concentrations from 10 pg/ml to 1 ng/ml (Fig. 2G). These studies indicated a high level of reproducibility as determined through statistical analysis of separate data
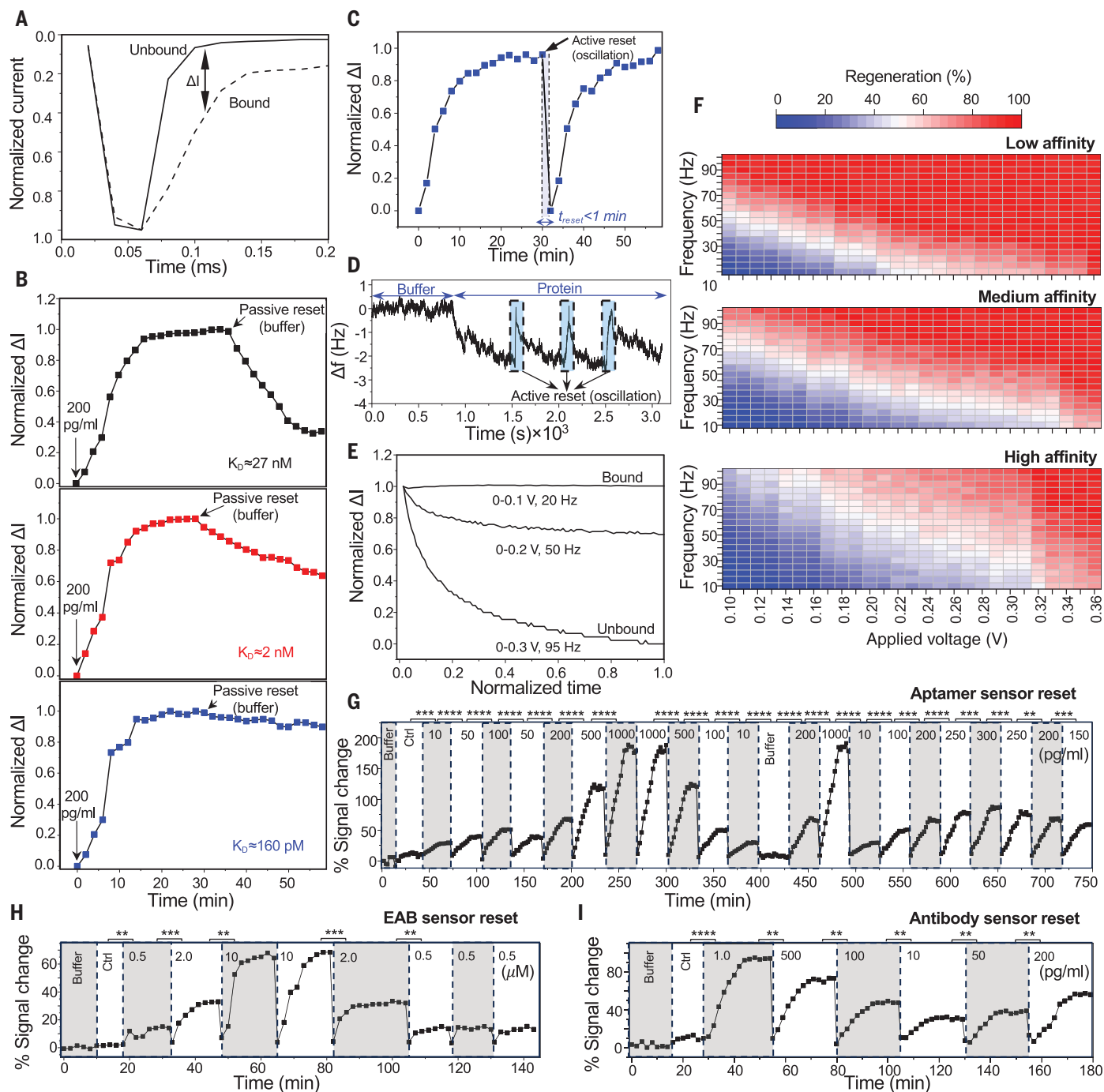
Fig. 2. Active-reset sensor development. (**A**) Chronoamperometry was used for the detection of target proteins that slow electron-transfer kinetics upon binding. (**B**) Measurement of a model protein (MPO) at a concentration of 200 pg/ml by using aptamers with K_d of 27 nM, 2 nM, and 160 pM (sequences and sources of aptamers are available in table S1). (**C**) Oscillation-based reset of the sensor for high-affinity MPO aptamer sensor in <1 min. (**D**) Confirmation of protein dissociation by use of QCM measurements. (**E**) Dependence of level of sensor reset on voltage and frequency applied. (**F**) Reset percentage based on frequency and applied voltage level for the MPO aptamers with low, medium, and high affinities. (**G**) In vitro continuous measurements by using a MPO aptamer sensor with 10 pg/ml to 1000 pg/ml concentrations in a 12+ hour

experiment. (**H**) Active reset applied to structure-switching electrochemical aptamer-based (EAB) sensors specific for doxorubicin, with square wave voltammetry used as the detection method. (**I**) Active reset applied to antibody-based molecular pendulum biosensor specific to IL-6. Statistical analysis was performed for the last five signal points of each concentration, which represents the statistically significant difference between various concentrations [P values are indicated with stars: **$P < 0.01$, ***$P < 0.001$, ****$P < 0.0001$; two-sided, two-sample t tests and analysis of variance (ANOVA)]. In (A) to (C) and (D), the current data and ΔI are normalized by their maximum value in the bound state. The time values in (E) are normalized with the maximum oscillation time for each case. All experiments were reproduced with $n > 3$ replicates.
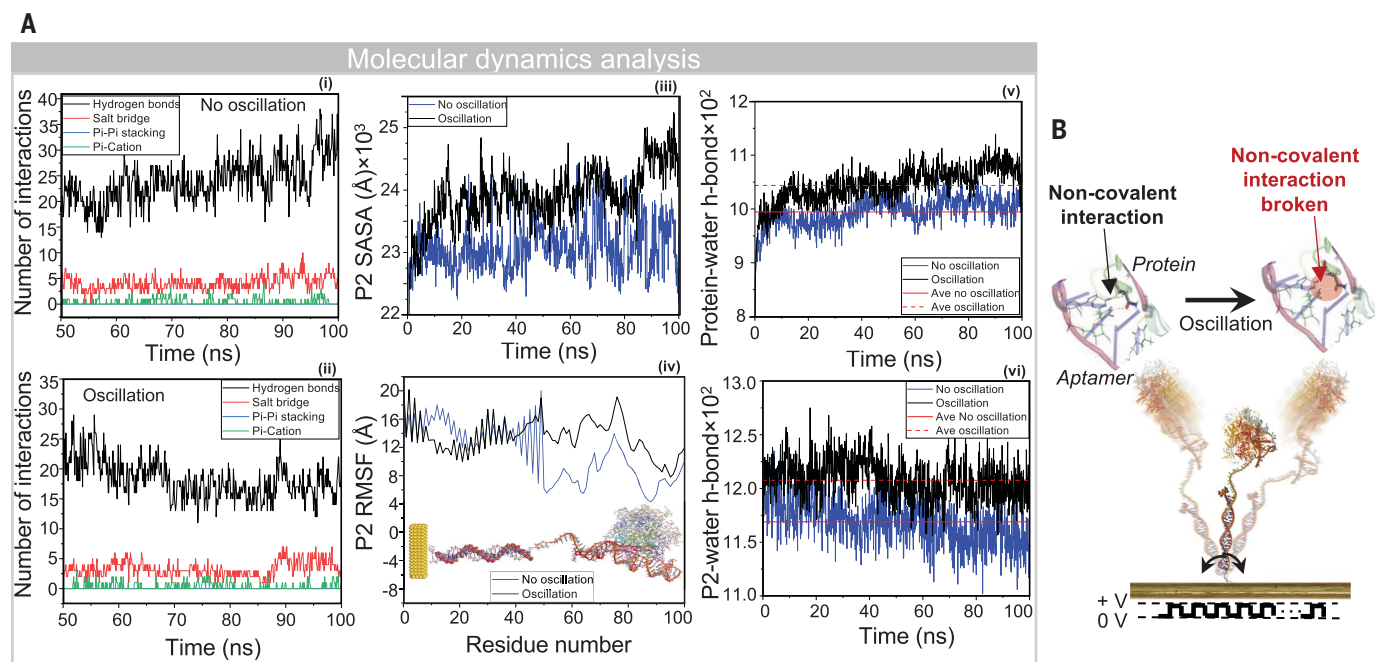
Fig. 3. MD simulations of oscillation-based reset. (**A**) MD analysis of an aptamer-protein complex in the absence and presence of oscillation. (i and ii) Computed number of interactions between aptamer and protein in the (i) absence and (ii) presence of oscillation. (iii) SASA of P2 aptamer in the complex state. (iv) RMSF values of P2 aptamer in the complex state. (v and vi) Hydrogen bond number between (v) protein and water molecules and (vi) P2 aptamer and water molecules. Ave, average. (**B**) Schematic showing proposed mechanism of oscillation-based sensor reset. Application of an alternating potential oscillates the sensor, which leads to breakage of noncovalent interactions and subsequent protein release.

points collected at the same concentration. This dataset also demonstrates the effectiveness of the active-reset approach when tracking increasing and decreasing concentrations.

We also investigated the universality of the method by applying the active-reset methodology to various target molecules of different sizes, sensing approaches, and receptor types (Fig. 2, H and I, and figs. S13 and S14). The results confirmed that the active-reset methodology is applicable to a wide range of sensors that use either aptamers or antibodies as receptor elements. This approach successfully targeted a variety of analytes, including small molecules such as serotonin, peptide-based hormones such as insulin, and larger proteins such as MPO.

To investigate the potential mechanisms that drive complex dissociation and sensor reset (Fig. 3A), we used molecular dynamics (MD) simulations to monitor the structural details of the aptamer-protein interaction and how oscillating potentials can affect complexation (Fig. 3B and figs. S15 to S21). We report in Fig. 3A, i and ii, on the quantity of noncovalent interactions between the aptamer and protein for scenarios with and without oscillation, with hydrogen bonding being the dominant mode of interaction.

The 100-ns simulation shows a decrease in average hydrogen bonds from 21.5 to 16.9 with oscillations (fig. S15). The solvent accessible surface area (SASA) of the aptamer increases significantly under oscillation (Fig. 3A, iii), which indicates greater exposure to water molecules, which may compete for protein binding. Root mean square fluctuation (RMSF) values in Fig. 3A, iv, reveal amplified fluctuations in the protein-binding domain (residues 55 to 117). There is an increased hydrogen bonding between water and protein/P2 (Fig. 3A, v and vi), which suggests improved solvation and reduced aptamer-protein interaction. The simulations indicate that rapid oscillation destabilizes the protein-bound sensor complex because of drag, inertial forces, and increased water collisions. Comparisons of high-energy (higher frequency/voltage) and low-energy (lower frequency/voltage) systems (figs. S22 to S25) further align with observed experimental behavior.

To further understand the relation of drag and inertial forces on the sensor reset performance, we oscillated the sensor in a solution with significantly increased viscosity (fig. S26). The higher viscosity leads to an increase in the drag force and a decrease in the inertial force as the sensor's angular displacement decreases during oscillation. By decreasing frequency and consequently increasing the inertial force, levels of reset increased (fig. S26). These experiments, combined with the observations of the MD simulations, indicate that the mechanism of sensor reset involves a variety of molecular forces imparted by the potential-induced oscillations.

Microdevices for electrochemical measurements in vivo

To test active-reset sensors for the intended application of continuous protein monitoring, an implantable device contacting dermal ISF was developed for electrochemical testing. ISF has emerged as a key biofluid for biomolecular analysis owing to its minimally invasive sampling, rapid equilibration with surrounding tissues, and high compositional correlation with blood (38, 39). However, despite its advantages, ISF has not gained widespread adoption in clinical applications because of its complex extraction methodologies and small volumes available for ex vivo analysis (40, 41). An alternative approach to ISF monitoring involves direct, in situ analysis of interstitial analytes by using sensor-integrated microneedles or microdevices that can be adapted to various form factors (22, 42).

We fabricated a microscale enclosure for wire-based electrodes that featured three channels for working, reference, and counter electrodes and a main central channel featuring three inlets within the tip of the device that are internally connected for ISF flow (Fig. 4A and fig. S28). ISF enters the microdevice through capillary flow through the inlets owing to its hydrophilicity and the overall design of the channels (figs. S28 and S29). Electrodes are embedded within the device, which ensures that the functionalized electrodes are protected during skin insertion (figs. S29 and S30).
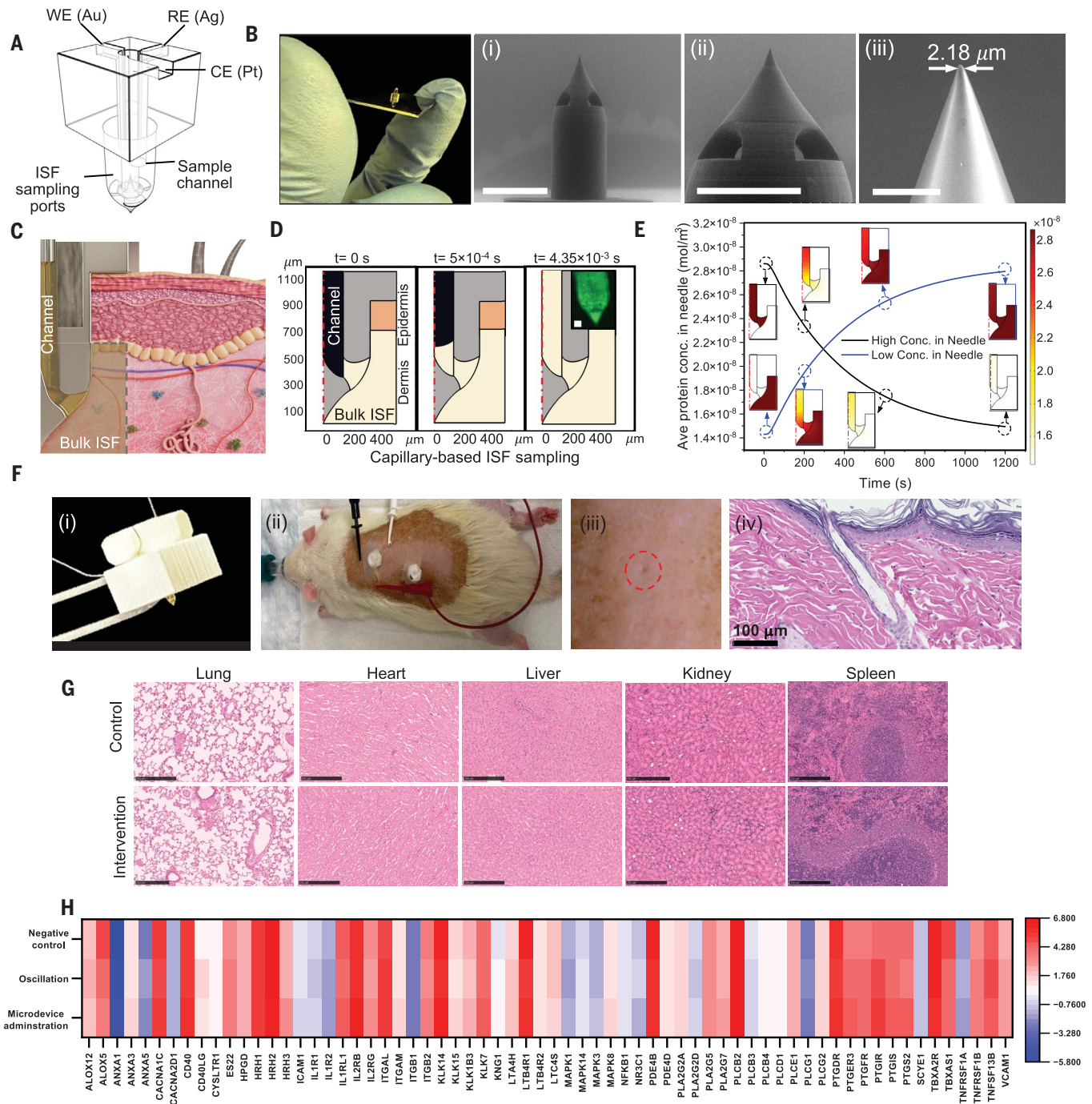
Fig. 4. Implantable sensor architecture, fluid dynamics, and biocompatibility.
(**A**) Schematic of fabricated microneedle. (**B**) Microneedle microscopy images showing (i) the microneedle side, (i) the printed inlet features, and (iii) the microneedle tip. Scale bars, (i and ii) 500 μm and (iii) 50 μm. (**C**) Illustration of ISF flowing into the microneedle through capillary force. (**D**) Computational fluid dynamic (CFD) simulation of the ISF flow when the dermis pressure is at its minimum (−4 mmHg) and requires <5 ms to fill the needle. (Inset) A fluorescence microscopy image of the filled microneedle. Scale bar, 300 μm. (**E**) CFD simulation of the protein concentration change. The average protein level in the microneedle is calculated over time when the concentration in the microneedle is lower or higher than in the dermis layer. This causes the proteins to diffuse into or out of the microneedle and equilibrate in <20 min. Conc., concentration. (**F**) Implanted microdevice. (i) The device mounted with housing for dermal implant. (ii) Administration of the sensing platforms on rat dorsal skin. (iii) Indentation caused by the microneedle penetration. (iv) H&E-stained tissue section of the rat after microneedle penetration, illustrating the extent of penetration. (**G**) H&E-stained sections of healthy rat organs with and without administration of the microdevice, indicating excellent biocompatibility of the device. Scale bar, 500 μm. (**H**) Quantitative polymerase chain reaction results of a comprehensive panel of 66 genes spanning crucial inflammatory pathways that were systematically investigated to discern any potential activation of inflammatory pathways.
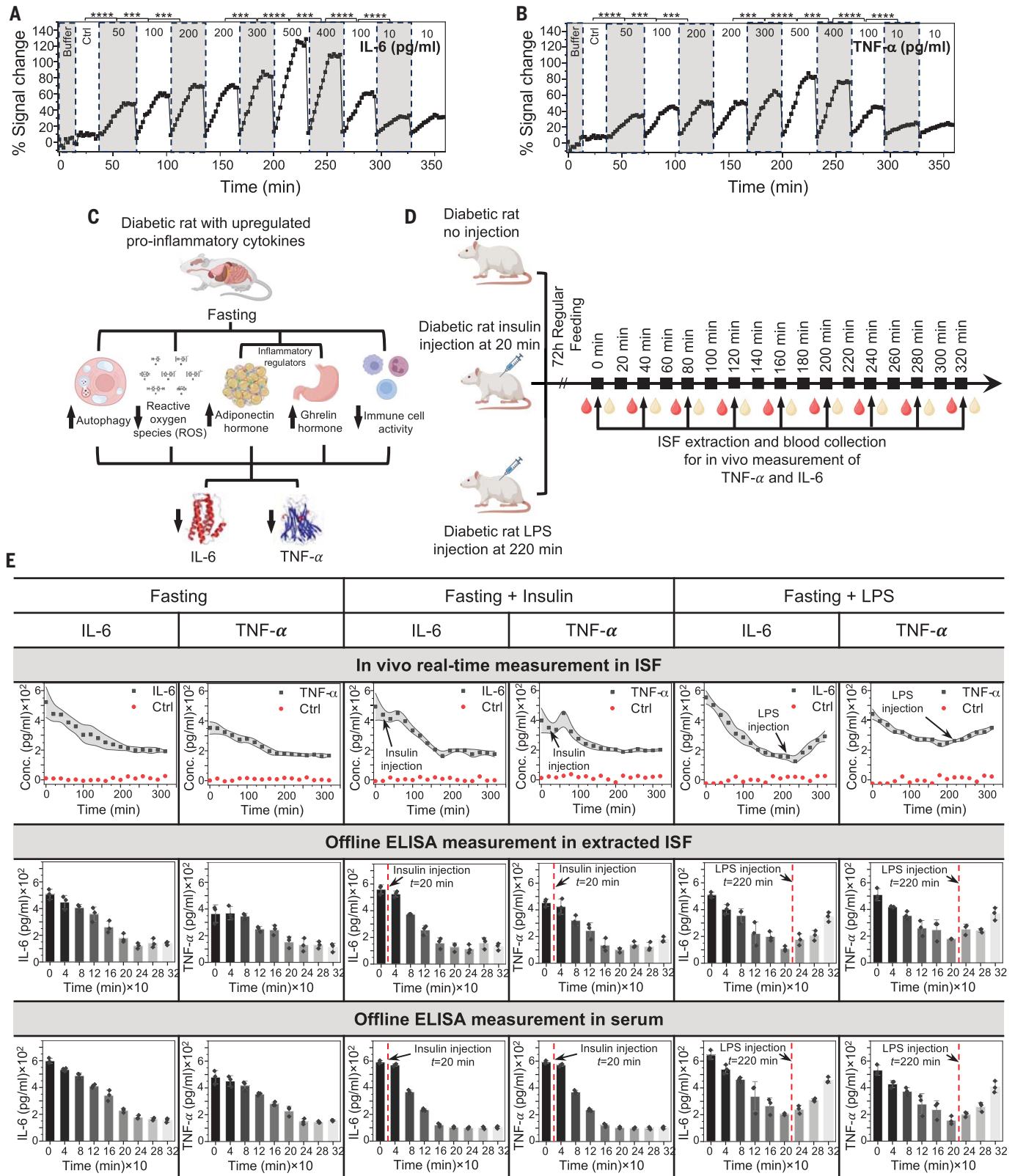
Fig. 5. Continuous monitoring of IL-6 and TNF-α in diabetic rats. (**A** and **B**) Real-time monitoring of IL-6 and TNF-α for about 6 hours for the biological target concentration range of 10 to 500 pg/ml. The statistical analysis was performed for the last five signal points of each concentration, which represents the statistically significant difference between various concentrations (P values

are indicated with stars: ***P < 0.001 and ****P < 0.0001; two-sided, two-sample t tests and ANOVA). The statistical nonsignificant differences are not shown. (**C**) Impact of fasting on proinflammatory cytokines. Fasting enhances autophagy, increases production of adiponectin and ghrelin, reduces ROS, and lowers immune cell activity. This combination leads to the down-regulation

of IL-6 and TNF-α. (**D**) Design of the animal study: longitudinal microdevice administration on diabetic rats and blood/ISF collection. Diabetic rats underwent fasting for 6 hours, and the levels of IL-6 and TNF-α were measured every 20 min during the experiment. Different animals underwent fasting alone, fasting + insulin injection at 20 min, and fasting + LPS injection at 220 min. (**E**) Results of the animal study. IL-6 and TNF-α levels were measured over time in ISF by using the electrochemical platform for the fasting-only model, fasting + insulin model, and fasting + LPS model. The results were compared with ELISA measurement in ISF (extracted hydrogel microneedle patch) and in serum. All experiments were reproduced with *n* > 3 replicates. Ctrl, control.

The Young's modulus of the printed needle is 3.1 GPa, which is sufficient for skin puncture (*22*). The ISF inlets were designed to be small enough to ensure sufficient capillary force for the collection of ISF and large enough to prevent blockage during insertion and measurement (Fig. 4B) (*43*). Fluid movement in the dermis follows a descending hydrostatic gradient, from positive capillary pressure (10.5 to 22.5 mmHg) to negative dermal pressure (−1 to −4 mmHg). To assess device performance, fluid flow was simulated assuming the worst-case dermal pressure of −4 mm Hg (Fig. 4C). The simulation shows that ISF fills the device within 5 ms, ensuring rapid immersion of electrodes (Fig. 4D). Fluorescent microscopy confirmed the complete filling of inner channels with fluorescent ISF (Fig. 4D, inset). Velocity profiles and pressure changes during filling are detailed in fig. S31. Controlled ISF flow is essential for consistent electrode wetting and repeatable sensing, so the device was designed with a 90° expansion acting as a capillary stop valve (fig. S32). Biocompatibility tests showed minimal cytotoxicity and minor changes in cell viability after 48 hours (fig. S33).

Protein concentration in microdevices changes because of diffusion and reaches equilibrium with exterior ISF over time. A concentration shift from 1000 to 500 pM takes about 20 min (Fig. 4E and fig. S34).

In the in vivo study, the microdevice with integrated electrodes was implanted into the rat's dorsal skin. Hematoxylin and eosin (H&E) staining of the puncture site confirmed successful penetration through the epidermis and insertion into the dermal layer (Fig. 4F). To evaluate systemic toxicity, we isolated vital organs (heart, liver, lungs, and kidneys) and performed H&E staining to assess immune cell infiltration after administration. No meaningful differences or histological abnormalities were found between tissues from control rats and those implanted with microdevices (Fig. 4G).

We also assessed whether the microdevice or its oscillations triggered localized inflammation by analyzing more than 60 genes related to inflammatory pathways, including adhesion molecules, tumor necorsis factor (TNF) receptors, and prostaglandin metabolism. No significant changes in gene expression were observed in skin tissues from control, preoscillation, and postoscillation groups (Fig. 4H).

Continuous protein monitoring of inflammatory markers in diabetic rats

In the diabetic population, the inflammatory cytokines interleukin-6 (IL-6) and TNF-α are known to be markers of vascular inflammation, which is a leading cause of morbidity and mortality for these patients (*44, 45*). Methods that monitor inflammatory biomarkers would enable management of chronic diseases such as diabetes and could be used as a means to control complications. We therefore used these two cytokines as a test case for continuous protein monitoring in a rat model of diabetes. Sensors were developed and characterized for IL-6 and TNF-α (figs. S1 to S3). High-affinity aptamers were used for both analytes that enabled the realization of pg/ml detection limits (*46, 47*), which corresponds to the physiological levels of these proteins (fig. S35 and table S1). The sensor reset strategy was effective with both sensors for >350 min, as shown in the experiments described in Fig. 5, A and B, and fig. S36, which were performed in simulated ISF in vitro.

In rats with diabetes, proinflammatory cytokine levels are elevated compared with those in healthy rats owing to hyperglycemia-induced cytokine release (*48*). Diabetes is characterized by impaired insulin secretion and sensitivity, which is exacerbated by oxidative stress, endoplasmic reticulum stress, pancreatic amyloid deposition, and ectopic lipid accumulation, all of which can trigger or worsen inflammation (*44, 45*). In type 1 diabetes mellitus (T1DM), inflammation in pancreatic islets (insulitis) progressively destroys insulin-producing β cells, which results in lifelong insulin dependence for affected individuals, often children or adolescents. Fasting can reduce inflammation by downregulating cytokines, improving metabolic health, and enhancing glucose and insulin control. This includes inducing autophagy, increasing adiponectin and ghrelin, and decreasing reactive oxygen species (ROS) and immune cell activity (Fig. 5C). We conducted an animal study to directly observe inflammation in diabetic rats, using IL-6 and TNF-α as inflammatory markers, and investigated the effects of insulin and lipopolysaccharide (LPS) injection (Fig. 5D). We assessed sensor biofouling with and without bovine serum albumin (fig. S37) and found no significant difference. All in vivo measurements included a negative control to monitor sensor drift and biofouling.

Using implanted sensors, we measured IL-6 and TNF-α in ISF every 20 min in diabetic rats' dorsal skin (Fig. 5E and fig. S38). We collected blood samples every 40 min for enzyme-linked immunosorbent assay (ELISA) confirmation. We also extracted dermal ISF every 40 min with a hydrogel microneedle patch and measured cytokine levels with ELISA (fig. S39). IL-6 in fasting diabetic rats decreased from ~520 pg/ml to ~190 pg/ml (Fig. 5E). Insulin-injected rats showed a temporary inflammatory response at 60 min owing to tissue trauma but then displayed an IL-6 decrease similar to that of untreated rats. Similar trends were observed for TNF-α (Fig. 5E).

LPS injection triggers an immune response, which causes proinflammatory cytokine release (*41*). We tested the microdevice's ability to monitor cytokine changes under fasting and LPS injection conditions (Fig. 5E). Comparing sensors with and without active reset shows that active reset effectively tracks sharp changes in protein level (fig. S40).

The cytokine levels measured with the microdevice align with offline ELISA results generated with ISF, and we observed consistent trends between electrochemical and ELISA measurements for ISF and serum (Fig. 5E). Bland-Altman analysis confirmed agreement between in vivo and offline ELISA measurements (fig. S41).

Different rates of cytokine level changes were observed in fasting-only, fasting + insulin, and fasting + LPS rats, with insulin accelerating cytokine reduction and LPS exacerbating inflammation (figs. S42 to S44). These findings validate the active-reset sensor's capability to track inflammatory biomarkers in vivo.

Conclusions

We developed an approach that enables real-time, continuous monitoring of protein biomarkers in ISF. Whereas previous efforts in wearable and implantable sensors have focused primarily on small molecules, this device offers a solution for protein biomarker analysis, which overcomes the limitations of slow dissociation times associated with affinity receptors. By using oscillation-based active sensor reset and reagentless molecular pendulum technology, this device facilitates real-time measurements with high sensitivity and specificity. The active sensor reset mechanism facilitates return to the unbound state within 1 min, which allows for continuous protein monitoring. The versatility of this platform is demonstrated by using a wide range of sensor architectures for the successful measurement of various protein and molecule biomarkers with different sizes and affinities, including cytokines, in an animal model of diabetes.

REFERENCES AND NOTES

1. C. D. Flynn *et al.*, *Nat. Rev. Bioeng.* **1**, 1–16 (2023).
2. Y. Li, N. Li, N. De Oliveira, S. Wang, *Matter* **4**, 1125–1141 (2021).
3. T. Young, V. Clark, N. Arroyo-Currás, J. Heikenfeld, *ECS Sens. Plus* **2**, 027001 (2023).
4. M. Poudineh *et al.*, *Nat. Biomed. Eng.* **5**, 53–63 (2021).

5. C. Parolo et al., ACS Sens. 5, 1877–1881 (2020).
6. P. Libby, Am. J. Clin. Nutr. 83, 456S–460S (2006).
7. K. E. Wellen, G. S. Hotamisligil, J. Clin. Invest. 115, 1111–1119 (2005).
8. A. L. Chu et al., Brain Behav. Immun. 95, 1–3 (2021).
9. S. B. Kim et al., Small 14, e1802876 (2018).
10. H. Y. Y. Nyein et al., ACS Nano 10, 7216–7224 (2016).
11. S. Li et al., ACS Nano 17, 18525–18538 (2023).
12. N. Arroyo-Currás et al., Proc. Natl. Acad. Sci. U.S.A. 114, 645–650 (2017).
13. J. S. Swensen et al., J. Am. Chem. Soc. 131, 4262–4266 (2009).
14. C. Zhao et al., Sci. Adv. 7, eabj7422 (2021).
15. C. Zhao et al., ACS Sens. 7, 3644–3653 (2022).
16. J. Li et al., Nature 606, 94–101 (2022).
17. B. Wang et al., Sci. Adv. 8, eabk0967 (2022).
18. C. Ye et al., Nat. Nanotechnol. 19, 330–337 (2024).
19. I. A. P. Thompson et al., Sci. Adv. 9, eadh4978 (2023).
20. W. Gao et al., Nature 529, 509–514 (2016).
21. M. Wang et al., Nat. Biomed. Eng. 6, 1225–1235 (2022).
22. F. Tehrani et al., Nat. Biomed. Eng. 6, 1214–1224 (2022).
23. A. Langer et al., Nat. Commun. 4, 2099 (2013).
24. H. Yousefi et al., J. Am. Chem. Soc. 143, 1722–1727 (2021).
25. Y. Luo et al., ACS Nano 17, 5211–5295 (2023).
26. J. Tu et al., Nat. Biomed. Eng. 7, 1293–1306 (2023).
27. D. Chang et al., Nat. Chem. 15, 773–780 (2023).
28. B. Jagannath et al., Bioeng. Transl. Med. 6, e10220 (2021).
29. S. Shahub et al., Inflamm. Bowel Dis. 2024, izae054 (2024).
30. R. P. Hirten et al., Biosens. Bioelectron. X 16, 100435 (2024).
31. J. Das et al., Nat. Chem. 13, 428–434 (2021).
32. H. Zargartalebi et al., J. Am. Chem. Soc. 144, 18338–18349 (2022).
33. A. Mahmud et al., Angew. Chem. Int. Ed. 62, e202213567 (2023).
34. H. Kaur, J. G. Bruno, A. Kumar, T. K. Sharma, Theranostics 8, 4016–4032 (2018).
35. N. Nakatsuka et al., Science 362, 319–324 (2018).
36. M. Lin et al., Angew. Chem. Int. Ed. 54, 2151–2155 (2015).
37. M. Lee, D. R. Walt, Anal. Biochem. 282, 142–146 (2000).
38. M. Friedel et al., Nat. Biomed. Eng. 7, 1541–1555 (2023).
39. J. Heikenfeld et al., Nat. Biotechnol. 37, 407–419 (2019).
40. M. Zheng et al., Adv. Healthc. Mater. 9, e1901683 (2020).
41. Z. Wang et al., Nat. Biomed. Eng. 5, 64–76 (2021).
42. S. Lin et al., Sci. Adv. 8, eabq4539 (2022).
43. Á. Cárcamo-Martínez et al., Int. J. Pharm. 599, 120455 (2021).
44. G. S. Hotamisligil, Nature 542, 177–185 (2017).
45. D. L. Eizirik, M. L. Colli, F. Ortis, Nat. Rev. Endocrinol. 5, 219–226 (2009).
46. M. Tertiş, B. Ciui, M. Suciu, R. Săndulescu, C. Cristea, Electrochim. Acta 258, 1208–1218 (2017).
47. E. W. Orava, N. Jarvik, Y. L. Shek, S. S. Sidhu, J. Gariépy, ACS Chem. Biol. 8, 170–178 (2013).
48. K. Esposito et al., Circulation 106, 2067–2072 (2002).

ACKNOWLEDGMENTS

SUPPLEMENTARY MATERIALS